Journal of Materials Chemistry A

Multimodal characterization of solution-processed Cu3SbS4 absorbers for thin film solar cells

Journal:	*Journal of Materials Chemistry A*
Manuscript ID	TA-ART-01-2018-000001.R2
Article Type:	Paper
Date Submitted by the Author:	18-Apr-2018
Complete List of Authors:	Albuquerque, Gustavo; Oregon State University, School of Chemical, Biological, and Environmental Engineering Kim, Ki-Joong; Oregon State University, School of Chemical, Biological and Environmental Engineering Lopez, Jonathon; Oregon State University, School of Chemical, Biological, and Environmental Engineering Devaraj, Arun; Pacific Northwest National Lab, Environmental Molecular Sciences lab Manandhar, Sandeep ; University of Texas at El Paso, Department of Mechanical Engineering Liu, Yi-Sheng; Lawrence Berkeley National Laboratory, Advanced Light Source Guo, Jinghua; Lawrence Berkeley National Laboratory, Chang, Chih-hung; Oregon State University, School of Chemical, Biological, and Environmental Engineering Herman, Gregory; Oregon State University, Sch. Chem, Bio and Env Eng

Multimodal characterization of solution-processed Cu_3SbS_4 absorbers for thin film solar cells

Gustavo H. Albuquerque[1], Ki-Joong Kim[2], Jonathon I. Lopez[1], Arun Devaraj[3], Sandeep Manandhar[4], Yi-Sheng Liu[5], Jinghua Guo[5], Chih-hung Chang[1], and Gregory S. Herman[1,*]

[1]Oregon State University, School of Chemical, Biological, and Environmental Engineering, Corvallis, Oregon, 97331, USA

[2]National Energy Technology Laboratory, U.S Department of Energy, Pittsburgh, Pennsylvania, 15236, USA

[3]Physical and Computational Sciences Directorate, Pacific Northwest National Laboratory, Richland, Washington, 99354, USA

[4]Department of Mechanical Engineering, University of Texas at El Paso, El Paso, Texas, 79968, USA

[5]Advanced Light Source, Lawrence Berkeley National Laboratory, Berkeley, California, 94720, USA

* Corresponding author: greg.herman@oregonstate.edu

Keywords

Cu_3SbS_4, Photovoltaics, XPS, XANES, Sulfurization

Abstract:

The most efficient inorganic thin film chalcogenide-based solar cells use CdTe or $CuInGaSe_2$ (CIGS) as absorber layers, which rely on toxic (Cd) and/or scarce elements (In, Te). The desire for more sustainable solar cells has led to the development of Earth abundant and non-hazardous chalcogenide absorbers. Cu_3SbS_4 (Famatinite) is a promising Earth abundant p-type semiconductor that has a low direct band gap (0.9-1.05 eV), is a superabsorber (absorption coefficient ~ 10^4-10^5 cm^{-1}), and has potential in low-cost, thin-film solar cells. Although these properties make the Cu_3SbS_4 phase stand out as a promising material for photovoltaics, to date Cu_3SbS_4 solar cells have only achieved

low efficiencies. In this study, we demonstrate a method for synthesizing Cu_3SbS_4 nanocrystals and formation of thin-films by coating nanocrystal precursors onto substrates. Optical, structural, and chemical state characterization were performed before and after thermal processing of the Cu_3SbS_4 films. A detailed experimental analysis of the bulk and surfaces of the Cu_3SbS_4 absorber films indicate that phase stability and preferential copper oxidation at the surface may limit device performance for Cu_3SbS_4 based solar cells. These findings may provide significant insight on how to improve Cu_3SbS_4 based solar cell performance by controlling processing conditions.

I. INTRODUCTION

Greenhouse gas emissions, scarcity of required minerals, increasing pollution, and global warming have forced changes in the world's energy usage and generation. Due to increasing demands for cleaner sources of energy, solar energy production in the U.S. has grown dramatically in the last decade.[1,2] Crystalline silicon (c-Si) is still the major commercial solar cell technology with solar conversion efficiencies (η) of 26.3 %, however other inorganic solar cell technologies have shown high efficiencies, including $Cu_2ZnSnS_{4-y}Se_y$ (η = 12.6 %), CdTe (η = 22.1 %), $CuIn_{1-y}Ga_ySe_2$ (η = 22.6 %), and GaAs (η = 28.8 %).[3]

Copper antimony sulfide (CAS) is a promising alternative to other inorganic absorbers, including CIGS and CdTe, for thin film solar cells.[2] Hybrid (inorganic-organic) perovskite-based devices have achieved high efficiencies (η = 22 %) but also rely on highly toxic elements such as lead.[4] CAS is a ternary I-V-VI semiconductor and contains relatively inexpensive and abundant elements that can form four major crystallographic phases including $CuSbS_2$ (Chalcostibite), $Cu_{12}Sb_4S_{13}$ (Tetrahedrite), Cu_3SbS_3 (Skinnerite), and Cu_3SbS_4 (Famatinite). The bandgap of these four CAS phases can vary from 0.5 to 2.0 eV, which is within the optimal theoretical range for high efficiency (η) single junction solar cells.[5,6] Several of the CAS compositions have been classified as superabsorbers, which potentially allow very thin and low-cost solar cells to be fabricated.[7] The high absorption coefficient for Cu_3SbS_4, in combination with its nearly optimal single junction band gap (~1.0 eV)[8] makes it a promising low-cost solar cell absorber material. Several studies have demonstrated solar cells for CAS, copper

antimony selenide (CASe), and Sb_2S_3 systems,[9–11] however all of these still have relatively low η. For example, CAS absorber layers deposited by vacuum-based methods, including sputter deposition Cu_3SbS_4,[12] atomic layer deposition $CuSbS_2$,[13] and thermal evaporation $CuSbS_2$[14,15] have η = 0.46, 0.02, and < 2 %, respectively. Much higher efficiencies were obtained for CAS absorber layers deposited by solution-based methods, where $CuSbS_2$ solar cells had η = 3.1 %[11,16,17] and Sb_2S_3 solar cells had η = 3 to 7.5 %.[11,18,19] More recently, sputter deposited $CuSbSe_2$ based solar cells have achieved η = 4.7 %,[20] however several other studies have fabricated Cu-Sb-S based solar cells with lower efficiencies than the earlier reported devices.[9,21,22] Most studies to date have focused on the structural and optical properties of several different CAS phases.[5,6,13,22–30] Very few studies have provided experimental or theoretical approaches that explain the low efficiencies observed for single junction $CuSbS_2$ solar cells.[31,32] To allow advances in CAS solar cell performance it is critical to understand what factors lead to the low efficiencies observed for CAS solar cells.

The use of nanoparticle inks is considered a promising, cost-effective approach to fabricate thin film solar cells at large scales.[33–37] Several studies have used solution-based approaches in the fabrication of high efficiencies solar cells, with performance exceeding those using vacuum-based processes.[16,38–41] In this study, we have used hot-injection methods to synthesize uniform Cu_3SbS_4 colloidal nanoparticles and Cu_3SbS_4 films were deposited using nanoparticle-based inks. We have characterized the structural, chemical, and optical properties of the Cu_3SbS_4 nanoparticles and thin films. The CAS films were analyzed after thermal annealing at a range of temperatures and environments using multimodal characterization methods, including Raman spectroscopy, UV-Vis

spectroscopy, X-ray diffraction (XRD), electron microscopy, X-ray absorption near edge spectroscopy (XANES), and X-ray photoelectron spectroscopy (XPS). These methods allowed us to characterize changes caused by thermal processing and identify factors that can be related to the low η achieved for CAS solar cells.

II. EXPERIMENTAL

A. Cu_3SbS_4 nanocrystals synthesis

All the reagents used in the CAS synthesis were stored in an N_2-filled glove box with oxygen and moisture concentrations below 0.5 ppm. Prior to storage the solvents were purged with N_2 for 60 min using flasks containing molecular sieves. Copper chloride (CuCl, 97 %) and antimony chloride ($SbCl_3.6H_2O$, 99.5 %) were obtained from Alfa Aesar. Sulfur precipitated powder was obtained from Fisher-Scientific. Chloroform was obtained from J.T. Baker (99.8 %). Oleylamine (OLA, ≥ 98 %) and 1-hexanethiol (95 %) were obtained from Sigma-Aldrich.

The synthesis of Cu_3SbS_4 nanocrystals was modified from a previously reported method.[42] In one flask, 1.4 mmol of copper chloride and 1.4 mmol of antimony chloride were dissolved in 22 mL of oleylamine. This mixture was heated to 85 °C while being vigorously stirred for about 15 min until the solution became clear. The clear solution was then transferred to a three-necked pear-shaped flask. In a second flask, 6.3 mmol of sulfur was added to 8 mL of oleylamine which was heated to 85°C while stirring for about 5 minutes. The three-necked pear-shaped flask containing the metal precursors was connected to a Schlenk line to degas the solution under low vacuum, followed by purging the reaction vessel with high purity argon. This alternating (degassing/purging) procedure

was repeated twice to remove most of the remaining nitrogen. A similar procedure was performed to the sulfur source flask. Finally, the metal precursor flask was heated to 200 °C, at which point the solution from the sulfur source flask was rapidly injected into the metal precursor solution. The initial temperature was maintained for 30 min. After cooling, the product liquor was transferred to centrifuge vials containing an equal volume of toluene. This liquid was centrifuged at 2400 rpm for 30 minutes and the supernatant was collected and purified using a liquid extraction process with methanol and increasing amounts of acetone. The nanoparticles were crashed out of solution with methanol, and then dispersed in toluene twice before being centrifuged at 4000 rpm in a mixture containing 7 mL of dispersed particles, 1 mL of acetone, and ~ 4 mL of methanol. After the purification steps, the particles were either characterized or used to prepare a nanoparticle ink with 20 wt.% CAS in 1-hexanethiol.

B. Film deposition and sulfurization process

The Cu_3SbS_4 nanoparticle inks were spin-coated at 3000 rpm for 10 s on 19 mm x 19 mm molybdenum coated glass substrates (200 nm Mo on 800 µm thick Eagle® 2000) or 20 mm x 20 mm quartz substrates (GM Associates, 1 mm of thickness). The CAS films were annealed in air in two steps: Step 1 was at 180°C for 2 min, and step 2 was at 280°C for 10 s. The spin-coating and annealing process was repeated 25 times to obtain films that were ~1 µm thick. The films were then annealed in a sulfur-rich atmosphere in a tube furnace. The substrates were mounted face down above an alumina crucible containing sulfur powder. The quartz tube (50 mm diameter) was purged with 50 mL/min of nitrogen. After one hour, the nitrogen flow rate was reduced to 12 mL/min. A 20 min.

total temperature ramping time was used for all anneals. Films were characterized within 24 hours of final preparation.

C. Characterization

XRD was performed using a Rigaku Ultima IV diffractometer ($\lambda_{Cu\text{-}K\alpha}$ = 0.1542 nm, 40 kV, 40 mA). Prior to XRD analysis of the CAS nanoparticles, they were drop cast onto glass slides and the solvent was evaporated in a N_2 environment. XRD analysis of the CAS films was performed after the indicated annealing steps. In all cases, XRD was performed using a fixed X-ray incidence angle (ω = 1.5 °). Raman spectra were obtained using a Horiba-Jobin Yvon HR-800 Raman spectrometer with an incident laser source (λ = 532 nm) where analysis was performed on the Mo substrates after using a needle to scrape off the CAS films. Absorbance measurements were obtained from CAS films deposited on quartz substrates using a Cary 5 UV-Vis-NIR spectrophotometer. Transmission electron microscopy (TEM), scanning transmission electron microscopy (STEM), and selected area electron diffraction (SAED) were obtained using a FEI Titan FEG with a 200 kV acceleration voltage. For TEM, STEM, and SAED, samples were prepared from Cu_3SbS_4 particles dispersed in a chloroform solution that was sonicated for 2 minutes (Branson model 2510 – Max power 130 W). The solution was then drop-cast onto a carbon coated copper grid, which was mounted in the microscope after drying for 5 minutes at 60°C. The Cu_3SbS_4 lattice spacing was estimated using 20 fringes from the high-resolution TEM (HRTEM) images. Scanning electron microscopy (SEM) imaging and energy dispersive X-ray spectroscopy (EDS) were performed using an FEI Quanta

600 FEG SEM with 5-30 kV accelerating voltage. EDS scans were taken in 4 different locations on the films, the average and standard deviation are provided in the chemical formula obtained by EDS. For cross section images the films were cleaved after being frozen in liquid N_2. XANES was performed at the Advanced Light Source, Lawrence Berkeley National Laboratory on Beamline 6.3.1.2. The energy resolution was set to 0.5 eV using a 1200 lines/mm grating. In these experiments, the Cu L_3 edge was analyzed and the base pressure of the experimental chamber was below $1x10^{-8}$ Torr. High purity copper metal was used as a reference and the spectra were energy corrected by fixing the Cu L_3 edge inflexion point at 932 eV.[43] Data were recorded in total fluorescence yield and total electron yield in order to obtain bulk and surface sensitive information, respectively.

XPS was performed using a Perkin-Elmer Phi 5600 MultiTechnique system with a monochromated Al Kα X-ray source (hν = 1486.6 eV). A 45° emission angle with respect to the sample surface was used for all measurements. The conditions for these measurements were 300 W X-ray power, 15.0 kV X-ray accelerating voltage, 0.8 mm x 2 mm analysis area, and a base pressure of 6×10^{-10} Torr. All samples were stored in a N_2-filled glove box prior to analysis. The spectrometer was calibrated to Au $4f_{7/2}$ and Cu $2p_{3/2}$ binding energies (E_b) at 84.00 and 932.66 eV, respectively.[44] CASA XPS software was used to fit the spectra using Shirley backgrounds. For each core-level the Gaussian/Lorentzian (G/L) peak shapes were determined by optimizing the relative ratio of the G/L for the low binding energy portion of the spectra.

The XPS E_b for the CAS films were calibrated using C 1s as a reference peak, which was set to 284.8 eV.[44] The Cu $2p_{3/2}$ peak was fit using a 90/10 G/L peak shape. No full

width half maximum (FWHM) constraints were used for copper due to the substantial difference in broadening between Cu, Cu^{+}, and Cu^{+2}, which has been observed previously.[45] The O 1s peaks were fit with an 80/20 G/L ratio. The same value was applied for the analysis performed for Sb $3d_{5/2}$ and $3d_{3/2}$. The intensity ratio of the Sb $3d_{5/2}$ to Sb $3d_{3/2}$ peaks were set to 3:2 with a peak separation of 9.35 eV. The S $2p_{3/2}$ and $2p_{1/2}$ peaks were fit using a 60/40 G/L peak shape. The intensity ratio of the S $2p_{3/2}$ to S $2p_{1/2}$ peaks were set to 2 with a peak separation of 1.2 eV.

III. RESULTS AND DISCUSSION

To evaluate the crystallographic phase and phase purity of the CAS nanoparticles we have used XRD. In Figure 1 we show an XRD pattern obtained from the as-synthesized nanocrystals. The main XRD peaks were observed at $2\theta = 29.0°$, 48.3°, and 57.2°, which correspond to diffraction from the (1 1 2), (2 0 4), and (3 1 2) crystallographic planes for the Cu_3SbS_4 structure. No XRD peaks were observed which would indicate the formation of impurity phases, such as copper sulfide, antimony sulfide, or the Tetrahedrite CAS phase. This result indicates that the synthetic procedure had high selectivity for nanocrystals with the desired Cu_3SbS_4 phase.

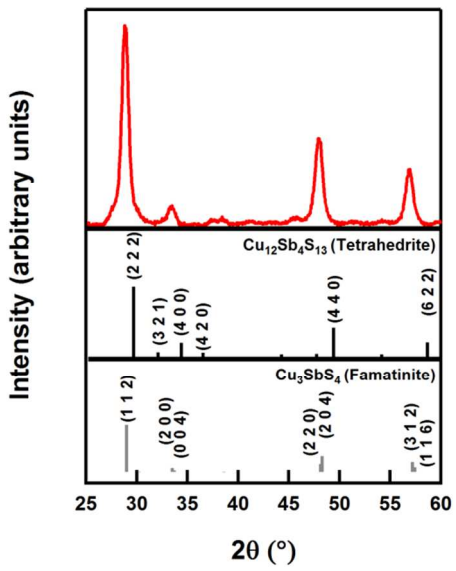

Figure 1: X-ray diffraction pattern of as-synthesized Cu_3SbS_4 nanoparticles. Patterns for $Cu_{12}Sb_4S_{13}$ [46] and Cu_3SbS_4 [47] were published elsewhere.

TEM, SAED, and STEM were used to characterize the as-synthesized Cu_3SbS_4 particles, as well as to determine the particle size distribution (PSD). Figure 2 (A) shows a high-resolution transmission electron microscopy (HRTEM) image of an individual Cu_3SbS_4 particle. The HRTEM image showed well-defined crystallographic planes, where the spacing was estimated to be 0.31 nm which corresponds to the (1 1 2) planes for the Cu_3SbS_4 lattice. Figure 2 (B) shows a SAED pattern, which was obtained from a group of particles. Diffraction spots associated with the (2 1 1), (2 2 4), and (3 2 1) crystallographic planes were observed. This set of data, in combination with the XRD results presented in Figure 1, allows us to confirm that Cu_3SbS_4 was the synthesized phase. In addition to crystallographic information, STEM images were obtained which are shown in Figure 2 (C). This data was also used to determine the PSD that are shown in Figure 2 (D). The measured PSD for the Cu_3SbS_4 particles indicated a 19 nm mean diameter, with a FWHM of 10 nm.

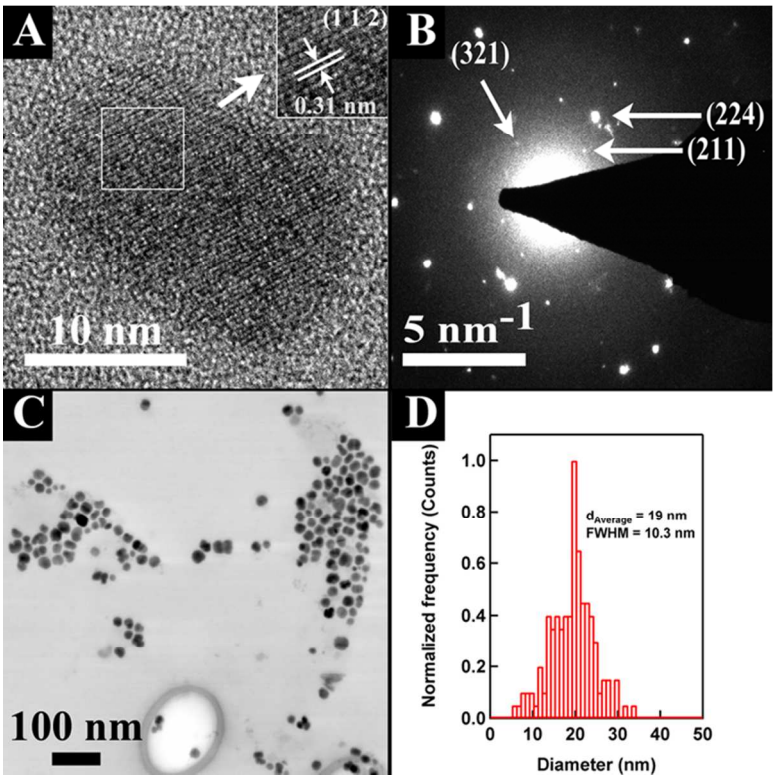

Figure 2: (A) HRTEM image of single Cu_3SbS_4 particle, (B) SAED of a group of Cu_3SbS_4 particles, (C) bright-field STEM image of as synthesized Cu_3SbS_4 particles, and (D) Particle size distribution obtained using the STEM image shown in (C).

Figure 3 shows a bulk ternary phase diagram for the Cu-Sb-S system at 300 ˚C. Several CAS compositions are shown on this plot, and indicates an excess of sulfur at a fixed temperature should result in a chemical potential that favors formation of Cu_3SbS_4.[48] Although deviations from this diagram should be expected for CAS nanocrystals due to segregation and size effects,[49–51] several studies have indicated that temperature and composition can yield different CAS phases or mixtures of CAS particles and copper sulfides.[5,23,42] In our synthetic approach, the 1:1 Cu/Sb composition led to the formation of Cu_3SbS_4 nanocrystals for T = 200, 220, 240 °C. Lower temperatures (170-190 °C) would result in the formation of $Cu_{12}Sb_4S_{13}$ as a major phase.

The excess sulfur was important for the formation of Cu_3SbS_4 since lower amounts of sulfur would lead to the formation of $CuSbS_2$. Based on this phase diagram, and the observations in the synthesis of Cu_3SbS_4 nanocrystals, we have evaluated the role of excess sulfur, annealing temperature, and annealing time to obtain phase pure Cu_3SbS_4. Although, high temperature sulfurization processes should increase the crystallinity of the CAS films, we kept the annealing times fairly short in our investigations to avoid formation of MoS_2 at the Cu_3SbS_4/Mo interface.

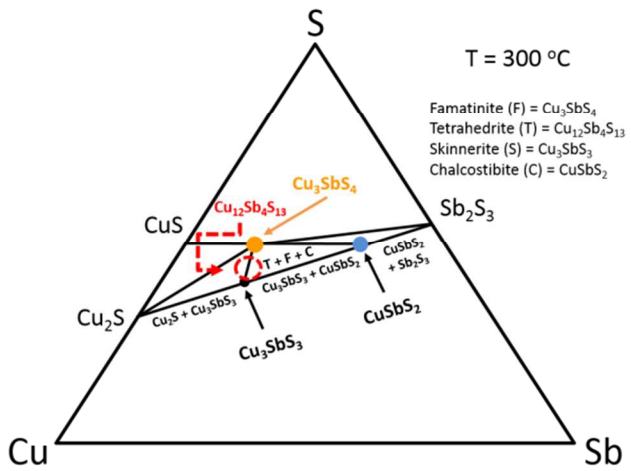

Figure 3: Ternary diagram for Cu, Sb, and S showing regions of formation of binary and ternary phases that can be formed at T = 300 °C.[48,52] (After Braga *et al.*)

Cu_3SbS_4 particles capped with oleylamine (OLA) were used to prepare dispersions of nanoparticle inks that were used to spin-coat CAS thin films. After spin-coating, the films were annealed in air to remove the capping agents. This was done to prevent formation of an undesired insulating layer surrounding the semiconducting particles. As a second step, a higher temperature anneal in a sulfur-rich atmosphere

(sulfurization) was used to enhance grain growth.[53] Figure 4 (A) provides XRD results for films after several different sulfurization processes. A phase change from Cu_3SbS_4 (Famatinite) to $Cu_{12}Sb_4S_{13}$ (Tetrahedrite) was observed, where the peak at $2\theta \approx 30°$, which is characteristic of the (2 2 2) crystallographic plane of $Cu_{12}Sb_4S_{13}$ phase, increased in intensity. This change was observed after annealing to 400 and 450 °C when 0.3 g of sulfur was used. Several studies have indicated that antimony sulfide sublimates at high temperatures, which can result in a phase change from Cu_3SbS_4 to $Cu_{12}Sb_4S_{13}$.[54,55] The Tetrahedrite phase is metallic, and must be avoided for solar cell applications.[7] Figure 4 (B) shows XRD results after using 5 g of S at 500°C for a 10 min anneal and is compared to the initial nanoparticle precursor after the anneal in air. The FWHM of the XRD peaks become much narrower after the sulfurization step, which indicates the formation of larger grains and consequently an increase in the crystallinity of the films. The increase in grain size and crystallinity is important to reduce grain boundaries and defects in the crystalline lattice, and ultimately results in CAS films with improved optical and electrical properties. A closer inspection of the XRD data in Figure 4 (B) indicated the formation of copper (II) sulfide, as indicated by the presence of the peak at $2\theta \approx 27.5°$, which is characteristic of the (1 0 1) crystallographic plane in CuS. We found that the sulfurization process significantly reduced the relative peak intensities ($I_{(h\,j\,k)}$) for CuS compared to the characteristic peaks for Cu_3SbS_4. As shown in Figure 4(B), the intensity ratio of the most intense peaks for each crystalline phase went from $I_{(101)\,CuS}/I_{(112)\,Cu_3SbS_4}$ = 28.3 % to 3.6 % after the sulfurization process.

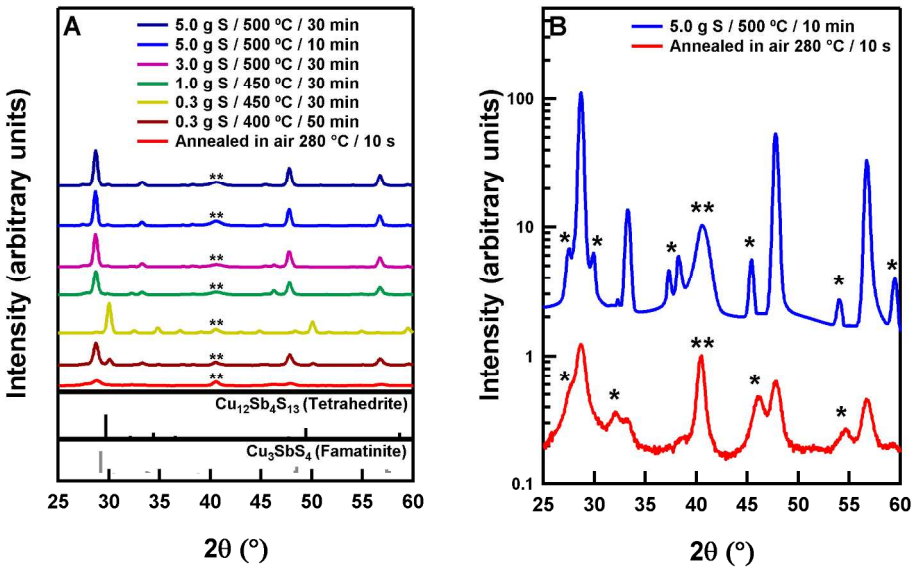

Figure 4: (A) X-ray diffraction data plotted on a linear scale for Cu_3SbS_4 films after air anneal only and after air anneal followed by different conditions of sulfurization. (B) X-ray diffraction data plotted on a log scale for Cu_3SbS_4 films prepared at optimized sulfurization condition and air anneal. Labeled peaks: (*) CuS [56] and (**) Mo. Patterns for $Cu_{12}Sb_4S_{13}$ [46] and Cu_3SbS_4 [47] were published elsewhere.

Figure 5 shows Raman spectra taken from the Mo substrate, after the optimized sulfurization process was performed (5 g S at 500 ^{o}C) for 10 and 30 minutes on the CAS films. Raman was performed in a region where the CAS films was removed and the results indicated that MoS_2 formation occurred after a 500 $^{\circ}$C anneal for 30 minutes, where two sharp peaks in the Raman spectrum at 384 cm^{-1} and 408 cm^{-1} match the expected Raman shifts for MoS_2.[57] A CAS film annealed for 10 minutes did not have Raman peaks associated with MoS_2.

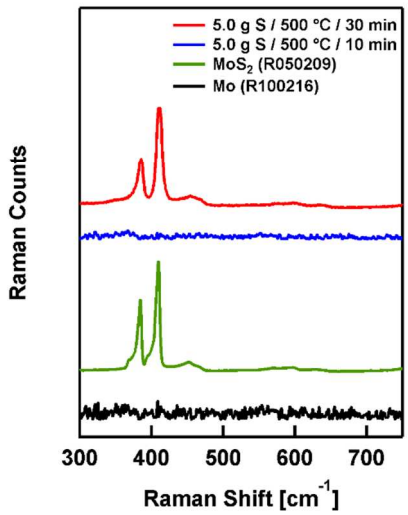

Figure 5: Raman spectroscopy of the Mo substrates after optimized Cu_3SbS_4 sulfurization processes. Reference spectra are part of the RRUFF database: MoS_2 (ID: R050209) and Mo (ID: R100216).

The uniform morphology of films for solar cell applications is very important and we have used SEM to monitor these changes for several different processing conditions. In Figure 6 we show SEM images of Cu_3SbS_4 films after several sulfurization conditions. In Figure 6 (A & B) there are distinct gaps located between Cu_3SbS_4 grains, which suggests material loss for annealing conditions > 500 °C and > 30 min. In Figure 6 (C) the Cu_3SbS_4 films are much more uniform after the optimized sulfurization condition (5 g S /500 °C/10 min) which suggests no material was lost during this annealing step. When comparing the samples before and after the optimized sulfurization process, the cross-section images in Figure 6 (D1 & D2) show the formation of large grains. However, even for the optimized sulfurization process, a layer of small grains and residual carbon from the capping agents remain in the film at the Mo/Cu_3SbS_4 interface. Therefore, we used a two-step annealing process to minimize the thickness of this interface layer to approximately 150 nm. For this process, we first annealed the Cu_3SbS_4 films to 280 °C

for 10 s in air, followed by a second anneal to 500 °C for 10 min with 5 g of S. EDS spectra of the films, shown in Figure 6 (D1 & D2), indicate that the film compositions were $Cu_{3.0\pm0.02}Sb_{1.0\pm0.08}S_{4.1\pm0.10}$ and $Cu_{3.2\pm0.10}Sb_{1.0\pm0.06}S_{4.3\pm0.20}$, respectively. The EDS results indicate that the films were both slightly copper and sulfur rich after sulfurization, which could indicate the formation of CuS. This is consistent with the XRD results discussed previously.

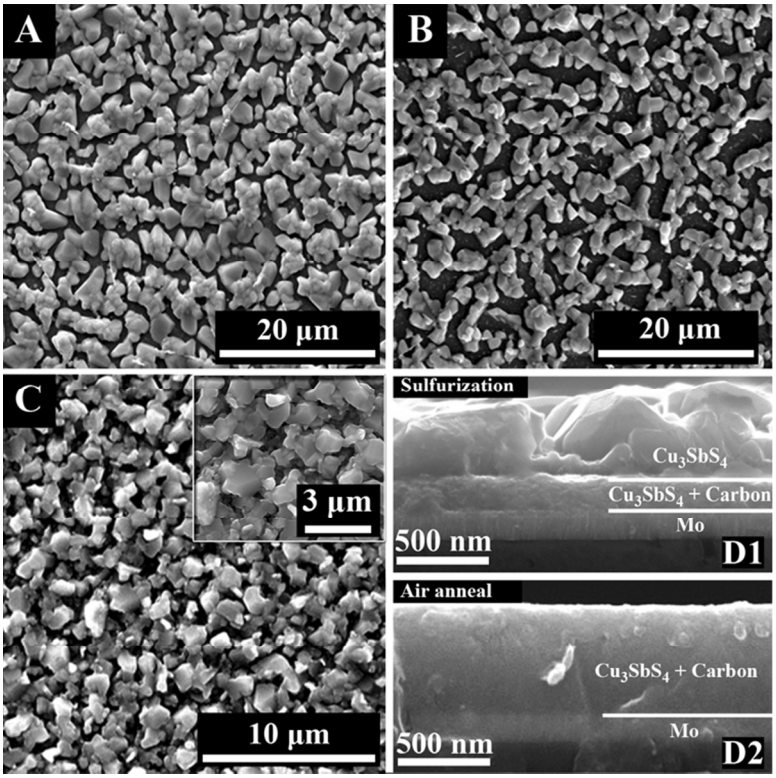

Figure 6: (A) Top-view SEM image of Cu_3SbS_4 film that underwent sulfurization at 500°C / 50 min + air anneal, (B) Top-view SEM image of Cu_3SbS_4 film that underwent sulfurization at 550°C / 30 min + air anneal, (C) Top-view SEM image of Cu_3SbS_4 film that underwent sulfurization at 500°C / 10 min + air anneal, (D1) Cross-section SEM image of Cu_3SbS_4 film that underwent sulfurization at 500°C / 10 min + air anneal, and (D2) Cross-section SEM image of Cu_3SbS_4 film that was only annealed in air.

As discussed above, the sulfurization process influences both the crystallographic structure and morphology of the films. We have also characterized the optical absorption properties for Cu_3SbS_4 films. Figure 7 shows optical absorption spectra for the Cu_3SbS_4

films before and after the optimal sulfurization process. In the inset in Figure 7, we show a Tauc plot that was obtained based on the absorption data. Both samples have high absorption coefficients (> 10^4 cm^{-1}) in the visible regime. A straight line between $(\alpha h\nu)^2$ and the photon energy indicates direct band gaps for both Cu_3SbS_4 samples. After sulfurization, there was a rapid increase in the absorption coefficient up to $1x10^4$ cm^{-1} right at the band edge (E_g ~ 0.9 eV) and continued up to $2.5x10^4$ cm^{-1} for $h\nu$ = 1.8 eV. The sulfurized sample also has a high absorption coefficient over a larger range of wavelengths compared to the air-annealed sample. The absorption coefficients of other inorganic absorbing materials at $h\nu$ = 1.8 eV are approximately $1.0x10^4$, $2.7x10^4$, and $3.3x10^4$ cm^{-1} for CdTe (E_g ~ 1.45 eV),[58–61] CIGS (E_g ~ 1.3 eV),[62,63] and CZTS (E_g ~ 1.50 eV),[64,65] respectively. In Figure 7 it can be seen that the Cu_3SbS_4 films also have a sub-band gap absorption with an absorption coefficient of ~$1.5x10^3$ cm^{-1}. The absorption spectra for the Cu_3SbS_4 samples can be attributed to different film stoichiometry across the film, the formation of copper sulfide, and the presence of defects at the grain boundaries, the interface between absorbing layer and substrate, and at the surface.[25,66–68] For example, CuS has absorption in the NIR range due to the presence of free carriers.[69,70]

The four crystalline phases $CuSbS_2$ (Chalcostibite), $Cu_{12}Sb_4S_{13}$ (Tetrahedrite), Cu_3SbS_3 (Skinnerite), and Cu_3SbS_4 (Famatinite) cover a wide range of band gaps (0.8 – 2.0 eV). Tetrahedrite is undesired for solar cell applications,[7] and Skinnerite can only be formed in a very narrow range of compositions (Figure 3), which would make it difficult to obtain phase pure samples after thermal treatment. Both $CuSbS_2$ (E_g ~ 1.6 eV) and Cu_3SbS_4 (E_g ~ 0.9 eV) nanocrystals have been synthesized with direct and indirect band

gaps.[5,16,23,42] However, both of these compositions have direct band gaps for bulk materials.[16,23,71] $CuSbS_2$ has the highest solar to electrical efficiencies for the CAS phases. However, the high absorption coefficient in the near-IR range and the rapid increase in absorption are of interest for tandem solar cell applications, where Cu_3SbS_4 could potentially be used as a bottom absorbing layer for commercially available CdTe solar cells. The use of lower or higher band gap materials can complement the absorption spectrum of an existing technology, and thereby improve the overall light harvesting and ultimately increase the total efficiency of the solar cell.[72–74] The increasing demand for lowering energy costs and reducing the environmental impact of chemical processes have guided development of sustainable materials and processes. A liquid-based deposition approach allows the scale up of thin film manufacturing while avoiding expensive vacuum-based processes.[40,75,76] The use of low-cost methods in the manufacturing of thin film solar cells, combined with the use of abundant and non-toxic materials with outstanding physical properties, would make Cu_3SbS_4 of high interest for the manufacturing of solar cells.

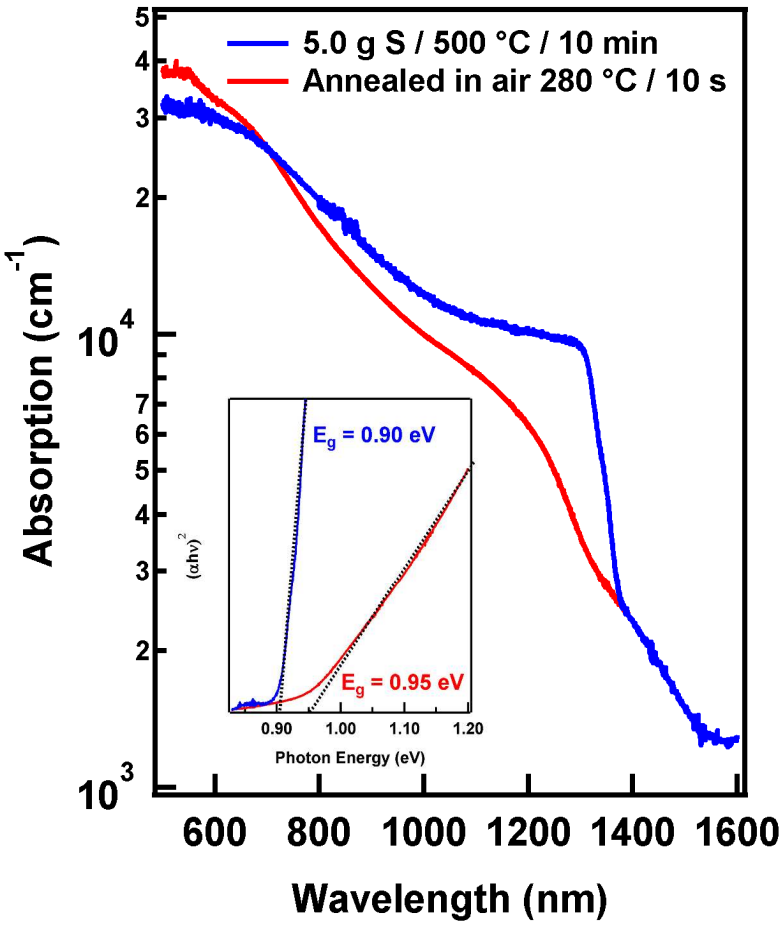

Figure 7: UV-Vis spectroscopy of films annealed in air only and annealed in air along with undergoing the optimized sulfurization process. Inset shows a plot of $(\alpha h\nu)^2$ vs photon energy (eV), where α represents the absorption coefficient.

The SEM cross sections in Figure 6 (D1 and D2) indicate that there are two distinct regions of the film with different morphologies. To better characterize the differences in the bulk and the surface of the Cu_3SbS_4 samples we have used Cu L-edge XANES. Figure 8 (A and B) shows Cu L-edge XANES data for Cu_3SbS_4 samples obtained using fluorescence (bulk sensitive) and the total electron yield (surface sensitive), respectively. We also show spectra for several reference samples (Cu metal, Cu_2S, and CuS) that correspond to different Cu oxidation states (i.e., Cu^0, Cu^+, and Cu^{2+},

which have the electronic configurations (Ar)$3d^{10}4s^1$, (Ar)$3d^{10}4s^0$, and (Ar)$3d^9 4s^0$, respectively). For higher oxidation states the partial occupation of the 3d orbitals permits dipole allowed absorption of X-rays corresponding to 2p-3d transitions.[43] Therefore, the pre-edge peak found at 931 eV should only be observed for samples containing Cu^{2+}, which is apparent in the spectra obtained for the CuS reference sample. This pre-edge peak was the major difference observed between our two Cu_3SbS_4 samples shown in Figure 8 (A). The air-annealed sample had a pre-edge feature, while the sample after the optimal sulfurization process did not. This data indicates that the optimal sulfurization process yields Cu^+ throughout the bulk of the film. In Figure 8 (B), the pre-edge feature was observed for both samples using total electron yield. Total electron yield is more surface sensitive than fluorescence detection, and indicates that Cu^{2+} is present at the surface of both Cu_3SbS_4 samples.

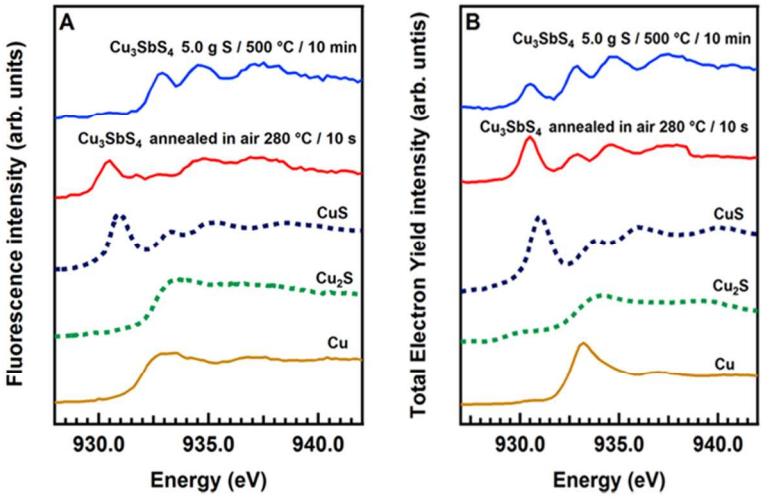

Figure 8: Cu L-edge XANES spectra from films after the air annealing process only and for films after the air annealing process and the optimized sulfurization process (10 minutes at 500 °C and using 5.0 g of sulfur). (A) Cu L-edge XANES results using fluorescence detection and (B) XANES results using total electron yield detection. References shown in dashed lines were published elsewhere.[43,77]

To further characterize the chemistry at the surface of the Cu_3SbS_4 samples we have performed XPS. Figure 9 (A & B) show Cu 2 $p_{3/2}$ XPS data obtained from Cu_3SbS_4 thin films before and after the optimal sulfurization process. The Cu $2p_{3/2}$ spectra had a major peak at E_b = 932.2 eV, and was fit using a FWHM of 1.1 eV. This binding energy is consistent with prior studies for Cu(I) that is present in Cu_3SbS_4.[23,78–80] A second peak was observed slightly higher at E_b = 934.8 eV, and was fit using a FWHM of 1.8 eV. This higher binding energy peak was assigned to sulfur rich copper sulfide (II) which was present primarily at the surface.[81] The difference in FWHM for the two peaks is consistent with the smaller FWHM observed for Cu^+ compared to Cu^{2+}.[45] In general, a small decrease in intensity for the copper (II) region at E_b = 934.6 eV, relative to the copper (I) peak at E_b = 932.2 eV, was observed after the sulfurization process. For Cu L-edge XANES, even for the total electron yield measurements, we found a substantial decrease in the Cu^{2+} pre-edge peak after sulfurization. Since XPS is much more surface sensitive than XANES, these results suggest that Cu^+ and Cu^{2+} are present at the surface both before and after the sulfurization process.

Figure 9 (C & D) shows Sb 3d and O 1s XPS data obtained from Cu_3SbS_4 thin films before and after the optimal sulfurization process. To fit the data, we initially started with the film after the sulfurization process, and focused on the Sb $3d_{3/2}$ component since there is no overlap with the O 1s peaks. Fitting the Sb 3d spectra resulted in two components with E_b = 530.0 eV (Sb $3d_{5/2}$) and 539.4 eV (Sb $3d_{3/2}$), which are consistent with prior assignments to Sb (V) in Cu_3SbS_4.[78] The absence of peaks at lower binding energies, such as E_b = 529.5 eV (Sb $3d_{5/2}$) and 538.6 eV (Sb $3d_{3/2}$), indicates that no antimony (III) sulfides were present in samples.[82,83] However, peaks at

higher E_b = 530.8 (Sb $3d_{5/2}$) and 540.2 eV (Sb $3d_{3/2}$) were also observed in the spectra, which are consistent with antimony (V) oxide.[84–86] After the sulfurization process, the intensity ratio for the Sb $3d_{5/2}$ components at E_b = 530.0 and 530.8 eV was higher which indicates an increase in the Cu_3SbS_4 phase compared to the Sb-O phase. In the Sb $3d_{5/2}$ spectra there are also peaks related to the O 1s core level. We used two O 1s peaks to obtain an adequate fit to the entire Sb 3d/O 1s spectra. These two components correspond to Sb-O bonds with E_b = 531.4 eV, and adsorbed oxygen containing species from the ambient with E_b = 531.9 eV.[87,88]

Figure 9 (E & F) show S 2p XPS spectra obtained from Cu_3SbS_4 thin films before and after the optimized sulfurization process. The S 2p spectra had clearly resolved doublets which correspond to S $2p_{3/2}$ and $2p_{1/2}$ with E_b = 161.7 and 163.0 eV, respectively. These binding energies have been assigned to S^{2-} that is present in Cu_3SbS_4.[78] Higher binding energy doublets were also observed with E_b = 163.4 eV (S $2p_{3/2}$) and 164.6 eV (S $2p_{1/2}$) before the sulfurization process. These doublets have been assigned to the formation of sulfur rich copper sulfide at the surface, where the higher electronegativity of sulfur results in a E_b shift to 163.9 eV (S $2p_{3/2}$) and 165.0 eV (S $2p_{1/2}$) due to reduction in the amount of copper and an increase in the number of S-S bonds.[81] A broad peak at E_b = 168.5 eV is due to the formation of sulfur oxides and its intensity was reduced after the sulfurization process.[81]

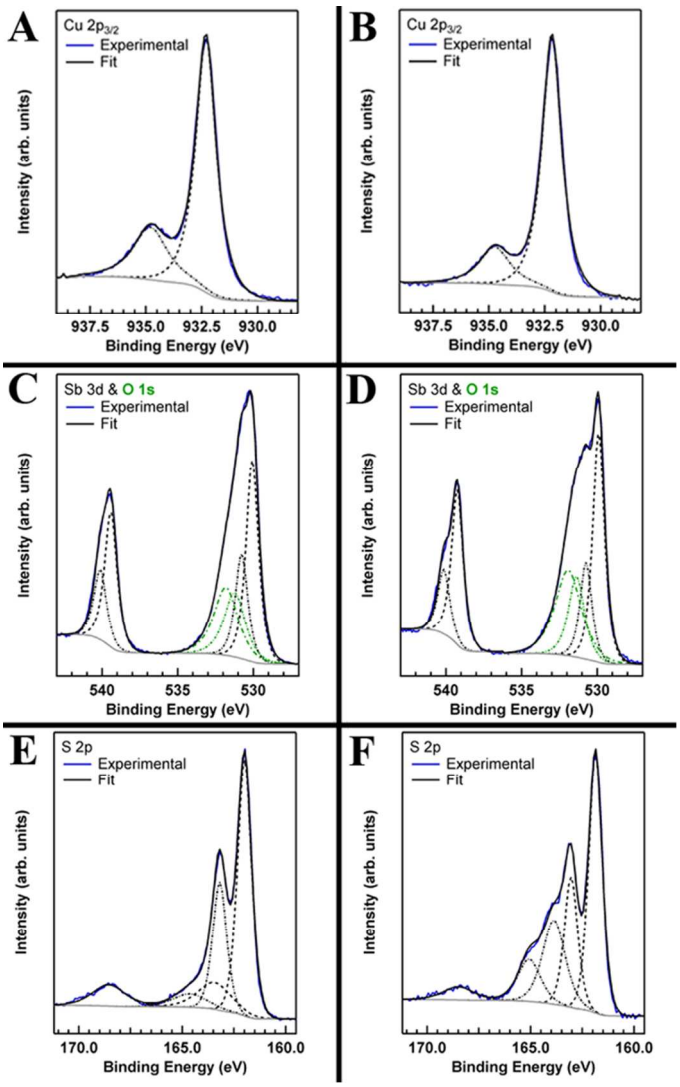

Figure 9: XPS spectra obtained from films after the air annealing process only (A,C, and E) and of films after the air annealing process and the optimized sulfurization process (sulfurization process performed for 10 minutes at 500 °C and using 5.0 g of sulfur) (B, D, and F).

Previous attempts at fabricating solar cells with a Cu_3SbS_4 absorbing layer has resulted in low efficiencies, with values as low as $\eta = 0.50$ %.[12] These low efficiencies could be caused by many factors including, changes in the Cu_3SbS_4 film composition at the surface after thermal processing, the formation of Cu^{2+} defects at the film surface, or surface oxidation. Inhomogeneities, growth orientation effects, and interface structural and electronic properties can all influence the efficiencies of solar cells.[89] The presence of CuS in the bulk of the films after annealing Cu_3SbS_4 samples in air, and the formation of

a CuS rich surface after the sulfurization process likely limits conversion efficiencies. The formation of CuS is due to decomposition of Cu_3SbS_4 during the thermal annealing processes, and has been identified in this study using XANES, XRD, and XPS. The formation of Sb-O at the surface also can limit solar cell efficiencies, and XPS indicated the presence of Sb-O even after the optimal sulfurization process. Prior studies have indicated that absorber layer surface chemistries can strongly affect the electronic properties of p-n junctions and therefore the efficiencies of solar cells.[69–72]

Ultimately, these chemical, structural, and compositional changes may be the main reasons why low photon to electron conversion efficiencies for Cu_3SbS_4 solar cells have been reported.

IV. CONCLUSIONS

In summary, solution-processed Cu_3SbS_4 thin films were successfully coated onto planar substrates. Optimization of the sulfurization process allowed improved crystallinity of Cu_3SbS_4 films, without formation of other CAS phases. EDS indicated that only small changes in the CAS stoichiometry were observed, even though both Cu_3SbS_4 and CuS were present in the films. SEM images indicated the formation of larger grains with uniform films after the optimal sulfurization process, however care must be taken during the anneal to prevent antimony sulfide sublimation. UV-Vis spectroscopy results indicated that the sulfurization process also increased the absorption coefficients of films in the visible and near-IR range. Cu L-edge XANES indicated that Cu_3SbS_4 films after an air anneal contained Cu^{2+} throughout the film, which agrees with

the EDS metal ratios and impurity peaks observed in XRD. After the optimal sulfurization process, XANES only detected Cu^{2+} using total electron yield, which indicates the formation of CuS only at the surface of the Cu_3SbS_4 films. XPS results from the Cu_3SbS_4 films indicated a reduction of the Cu^{2+}/Cu^{+} ratio after the sulfurization process, with a significant shift in the S 2p spectra suggesting formation of $Cu_{1-x}S_x$. The structural and composition changes at the Cu_3SbS_4 surface, such as formation of Cu^{2+}, can strongly influence solar cell performance and potentially limit efficiencies. The results of this study describe a low-cost deposition and processing methods to form Cu_3SbS_4 films, and identifies several issues that may limit Cu_3SbS_4 solar cell efficiencies.

ACKNOWLEDGMENTS

This research was funded by the United States National Science Foundation – Scalable Nanomanufacturing program (Grant CBET-1449383). A portion of this research was performed at the Northwest Nanotechnology Infrastructure, a member of the National Nanotechnology Coordinated Infrastructure, which is supported by the National Science Foundation (Grant ECCS-1542101). The acquisition of the OSU Titan TEM was supported by the National Science Foundation via the Major Research Instrumentation (MRI) program under Grant No. 1040588, the Murdock Charitable Trust, and the Oregon Nanoscience and Microtechnologies Institute (ONAMI). XANES spectra were obtained through an approved program user proposal at the Advanced Light Source, which is a DOE Office of Science User Facility under contract no. DE-AC02-05CH11231. The ALS approved program user proposal beam time was obtained through the chemical imaging

initiative, an LDRD program at PNNL. We acknowledge Trey Diulus and Dr. Igor Lyubinetsky for their assistance with the XPS experiments.

Table of Contents

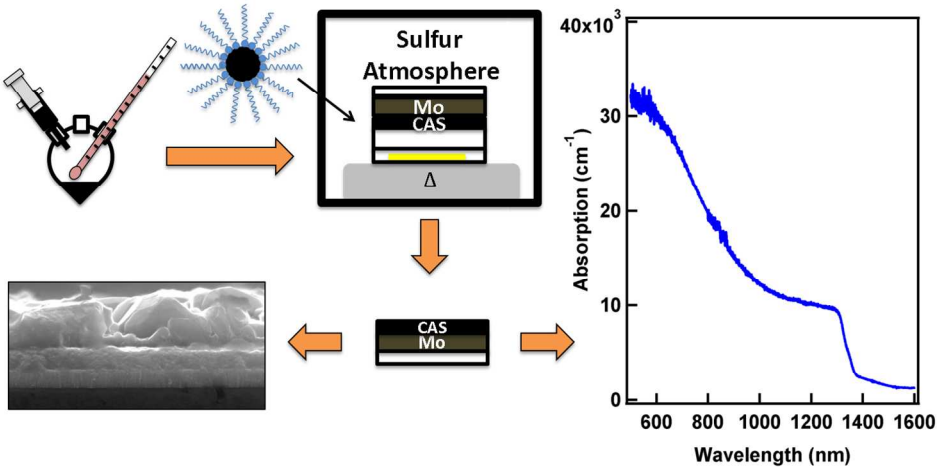

Optimized sulfurization process and final spectrum of the absorption coefficient of the Cu_3SbS_4 thin films.

REFERENCES

1. "Primary Energy Production by Source", U.S. Energy Information Administration (EIA), Monthly Energy Review, January of 2017.
2 N. Ali, A. Hussain, R. Ahmed, M. K. Wang, C. Zhao, B. U. Haq and Y. Q. Fu, *Renew. Sustain. Energy Rev.*, 2016, **59**, 726–737.
3 M. A. Green, K. Emery, Y. Hishikawa, W. Warta and E. D. Dunlop, *Prog. Photovolt. Res. Appl.*, 2016, **24**, 3–11.
4 S. Yang, W. Fu, Z. Zhang, H. Chen and C.-Z. Li, *J. Mater. Chem. A*, 2017, **5**, 11462–11482.
5 K. Ramasamy, H. Sims, W. H. Butler and A. Gupta, *Chem. Mater.*, 2014, **26**, 2891–2899.
6 A. Cho, S. Banu, K. Kim, J. H. Park, J. H. Yun, J.-S. Cho and J. Yoo, *Sol. Energy*, 2017, **145**, 42–51.
7 J. Heo, R. Ravichandran, C. F. Reidy, J. Tate, J. F. Wager and D. A. Keszler, *Adv. Energy Mater.*, 2015, **5**, 1401506.
8 L. Shi, C. Wu, J. Li and J. Ding, *J. Alloys Compd.*, 2017, **694**, 132–135.
9 L. Wan, C. Ma, K. Hu, R. Zhou, X. Mao, S. Pan, L. H. Wong and J. Xu, *J. Alloys Compd.*, 2016, **680**, 182–190.
10 B. Yang, C. Wang, Z. Yuan, S. Chen, Y. He, H. Song, R. Ding, Y. Zhao and J. Tang, *Sol. Energy Mater. Sol. Cells*, 2017, **168**, 112–118.
11 Y. C. Choi, D. U. Lee, J. H. Noh, E. K. Kim and S. I. Seok, *Adv. Funct. Mater.*, 2014, **24**, 3587–3592.
12 N. D. Franzer, N. R. Paudel, C. Xiao and Y. Yan, in *Photovoltaic Specialist Conference (PVSC), 2014 IEEE 40th*, IEEE, 2014, 2326–2328.
13 S. C. Riha, A. A. Koegel, J. D. Emery, M. J. Pellin and A. B. F. Martinson, *ACS Appl. Mater. Interfaces*, 2017, **9**, 4667–4673.
14 V. Vinayakumar, S. Shaji, D. Avellaneda, T. K. Das Roy, G. A. Castillo, J. A. A. Martinez and B. Krishnan, *Sol. Energy Mater. Sol. Cells*, 2017, **164**, 19–27.
15 F. W. de Souza Lucas, A. W. Welch, L. L. Baranowski, P. C. Dippo, H. Hempel, T. Unold, R. Eichberger, B. Blank, U. Rau, L. H. Mascaro and A. Zakutayev, *J. Phys. Chem. C*, 2016, **120**, 18377–18385.
16 S. Banu, S. J. Ahn, S. K. Ahn, K. Yoon and A. Cho, *Sol. Energy Mater. Sol. Cells*, 2016, **151**, 14–23.
17 W. Septina, S. Ikeda, Y. Iga, T. Harada and M. Matsumura, *Thin Solid Films*, 2014, **550**, 700–704.
18 C. P. Liu, Z. H. Chen, H. E. Wang, S. K. Jha, W. J. Zhang, I. Bello and J. A. Zapien, *Appl. Phys. Lett.*, 2012, **100**, 243102.
19 C. P. Liu, H. E. Wang, T. W. Ng, Z. H. Chen, W. F. Zhang, C. Yan, Y. B. Tang, I. Bello, L. Martinu, W. J. Zhang and S. K. Jha, *Phys. Status Solidi B*, 2012, **249**, 627–633.
20 A. W. Welch, L. L. Baranowski, H. Peng, H. Hempel, R. Eichberger, T. Unold, S. Lany, C. Wolden and A. Zakutayev, *Adv. Energy Mater.*, 2017, **7**, 1601935.
21 S. Yuan, H. Deng, X. Yang, C. Hu, J. Khan, W. Ye, J. Tang and H. Song, *ACS Photonics*, 2017, **4**, 2862–2870.

22 C. Macías, S. Lugo, Á. Benítez, I. López, B. Kharissov, A. Vázquez and Y. Peña, *Mater. Res. Bull.*, 2017, **87**, 161–166.
23 J. van Embden and Y. Tachibana, *J. Mater. Chem.*, 2012, **22**, 11466.
24 A. W. Welch, P. P. Zawadzki, S. Lany, C. A. Wolden and A. Zakutayev, *Sol. Energy Mater. Sol. Cells*, 2015, **132**, 499–506.
25 U. Chalapathi, B. Poornaprakash and S.-H. Park, *Ceram. Int.*, 2017, **43**, 5229–5235.
26 F. E. Loranca-Ramos, C. J. Diliegros-Godines, R. S. González and M. Pal, *Appl. Surf. Sci.*, 2018, **427**, 1099-1106.
27 J. Bincy, G. S. G. and L. R. A., *Mater. Res. Bull.*, 2017, **95**, 267–276.
28 W. Wang, L. Hao, W. Zhang, Q. Lin, X. Zhang and Z. Tang, *J. Mater. Sci. Mater. Electron.*, 2017, *In Press*.
29 Y. Zhang, J. Tian, K. Jiang, J. Huang, H. Wang and Y. Song, *Mater. Lett.*, 2017, **209**, 23–26.
30 S. Moosakhani, A. A. Sabbagh Alvani, R. Mohammadpour, P.-M. Hannula, Y. Ge and S.-P. Hannula, *Mater. Lett.*, 2017, *In Press*.
31 T. J. Whittles, T. D. Veal, C. N. Savory, A. W. Welch, F. W. de Souza Lucas, J. T. Gibbon, M. Birkett, R. J. Potter, D. O. Scanlon, A. Zakutayev and V. R. Dhanak, *ACS Appl. Mater. Interfaces*, 2017, **9**, 41916–41926.
32 F. Willian de Souza Lucas, H. Peng, S. Johnston, P. C. Dippo, S. Lany, L. H. Mascaro and A. Zakutayev, *J Mater Chem A*, 2017, **5**, 21986–21993.
33 S. Engberg, K. Agersted, A. Crovetto, O. Hansen, Y. M. Lam and J. Schou, *Thin Solid Films*, 2017, **628**, 163–169.
34 Y. Feng, K.-J. Jiang, J.-H. Huang, H.-J. Wang, M.-G. Chen, Y. Zhang, L. Zheng and Y.-L. Song, *Thin Solid Films*, 2017, **636**, 639–643.
35 Y. Qu, G. Zoppi and N. S. Beattie, *Prog. Photovolt. Res. Appl.*, 2016, **24**, 836–845.
36 Y. Qu, G. Zoppi and N. S. Beattie, *Sol. Energy Mater. Sol. Cells*, 2016, **158**, 130–137.
37 S. Sankaran, K. Glaser, S. Gärtner, T. Rödlmeier, K. Sudau, G. Hernandez-Sosa and A. Colsmann, *Org. Electron.*, 2016, **28**, 118–122.
38 W. Wang, F. Strössner, E. Zimmermann and L. Schmidt-Mende, *Sol. Energy Mater. Sol. Cells*, 2017, **172**, 335–340.
39 T. Zhang, Y. Yang, D. Liu, S. C. Tse, W. Cao, Z. Feng, S. Chen and L. Qian, *Energy Env. Sci*, 2016, **9**, 3674–3681.
40 Q. Guo, G. M. Ford, W.-C. Yang, B. C. Walker, E. A. Stach, H. W. Hillhouse and R. Agrawal, *J. Am. Chem. Soc.*, 2010, **132**, 17384–17386.
41 K.-J. Kim, C. Pan, S. Bansal, R. Malhotra, D.-H. Kim and C.-H. Chang, *Sustain. Energy Fuels*, 2017, **1**, 267–274.
42 S. Ikeda, S. Sogawa, Y. Tokai, W. Septina, T. Harada and M. Matsumura, *RSC Adv*, 2014, **4**, 40969–40972.
43 M. Grioni, J. B. Goedkoop, R. Schoorl, F. M. F. De Groot, J. C. Fuggle, F. Schäfers, E. E. Koch, G. Rossi, J.-M. Esteva and R. C. Karnatak, *Phys. Rev. B*, 1989, **39**, 1541.
44 J. F. Moulder, W. F. Stickle, P. E. Sobol and K. D. Bomben, *Handbook of X-ray Photoelectron Spectroscopy*, Perkin-Elmer Corporation, Eden Prairie., 1992.
45 D. Tahir and S. Tougaard, *J. Phys. Condens. Matter*, 2012, **24**, 175002.
46 R. C. Peterson and I. Miller, *Mineral. Mag.*, 1986, **50**, 717–721.
47 A. Pfitzner and T. Bernert, *Z. Krist.*, 2004, **219**, 20–26.

48 M. H. Braga, J. A. Ferreira, C. Lopes and L. F. Malheiros, in *Materials Science Forum*, Trans Tech Publ, 2008, **587**, 435–439.
49 M. Cui, H. Lu, H. Jiang, Z. Cao and X. Meng, *Sci. Rep.*, 2017, **7**, 41990.
50 G. Guisbiers, R. Mendoza-Pérez, L. Bazán-Díaz, R. Mendoza-Cruz, J. J. Velázquez-Salazar and M. José-Yacamán, *J. Phys. Chem. C*, 2017, **121**, 6930–6939.
51 Y. Magnin, A. Zappelli, H. Amara, F. Ducastelle and C. Bichara, *Phys. Rev. Lett.*, 2015, **115**, 205502.
52 B. J. Skinner, F. D. Luce and E. Makovicky, *Econ. Geol.*, 1972, **67**, 924–938.
53 H. Katagiri, K. Jimbo, W. S. Maw, K. Oishi, M. Yamazaki, H. Araki and A. Takeuchi, *Thin Solid Films*, 2009, **517**, 2455–2460.
54 B. Yang, L. Wang, J. Han, Y. Zhou, H. Song, S. Chen, J. Zhong, L. Lv, D. Niu and J. Tang, *Chem. Mater.*, 2014, **26**, 3135–3143.
55 A. W. Welch, L. L. Baranowski, P. Zawadzki, C. DeHart, S. Johnston, S. Lany, C. A. Wolden and A. Zakutayev, *Prog. Photovolt. Res. Appl.*, 2016, **24**, 929–939.
56 Y. L. Auyoong, P. L. Yap, X. Huang and S. B. A. Hamid, *Chem. Cent. J.*, 2013, **7**, 67.
57 A. Fairbrother, V. Izquierdo-Roca, X. Fontané, M. Ibáñez, A. Cabot, E. Saucedo and A. Pérez-Rodríguez, *CrystEngComm*, 2014, **16**, 4120.
58 K. Mitchell, A. L. Fahrenbruch and R. H. Bube, *J. Appl. Phys.*, 1977, **48**, 829–830.
59 M. S. Leite, M. Abashin, H. J. Lezec, A. Gianfrancesco, A. A. Talin and N. B. Zhitenev, *ACS Nano*, 2014, **8**, 11883–11890.
60 O. K. Echendu, F. B. Dejene and I. M. Dharmadasa, *J. Mater. Sci. Mater. Electron.*, 2017, **28**, 14615–14630.
61 A. A. Al-Ghamdi, S. A. Khan, A. Nagat and M. S. Abd El-Sadek, *Opt. Laser Technol.*, 2010, **42**, 1181–1186.
62 Y. Liu, D. Kong, H. You, C. Zhao, J. Li and J. Brugger, *ECS Solid State Lett.*, 2012, **1**, 26–28.
63 Y. Lian, J. Zhang, X. Ma, P. Yang and M. An, *Ceram. Int.*, 2018, **44**, 2599–2602.
64 C. Malerba, F. Biccari, C. L. Azanza Ricardo, M. Valentini, R. Chierchia, M. Müller, A. Santoni, E. Esposito, P. Mangiapane, P. Scardi and A. Mittiga, *J. Alloys Compd.*, 2014, **582**, 528–534.
65 K. Tanaka, M. Oonuki, N. Moritake and H. Uchiki, *Sol. Energy Mater. Sol. Cells*, 2009, **93**, 583–587.
66 A. Meeder, D. F. Marrón, A. Rumberg, M. C. Lux-Steiner, V. Chu and J. P. Conde, *J. Appl. Phys.*, 2002, **92**, 3016–3020.
67 P. Chattopadhyay, B. Karim and S. Guha Roy, *J. Appl. Phys.*, 2013, **114**, 243506.
68 I. Bonalde, E. Medina, M. Rodríguez, S. M. Wasim, G. Marín, C. Rincón, A. Rincón and C. Torres, *Phys. Rev. B*, 2004, **69**, 195201.
69 I. Grozdanov and M. Najdioski, *Journal of Solid State Chemistry*, 1995, **116**, 469–475.
70 L. Xiao, J. Wu, J. Ran, Y. Liu, W. Qiu, F. Lu, F. Shao, D. Tang and P. Peng, *AIP Adv.*, 2016, **6**, 085122.
71 A. Rabhi and M. Kanzari, *Chalcogenide Lett.*, 2011, **8**, 255–262.
72 C. Gao, M. Xu, B. K. Ng, L. Kang, L. Jiang, Y. Lai and F. Liu, *Mater. Lett.*, 2017, **195**, 186–189.
73 T. K. Todorov, D. M. Bishop and Y. S. Lee, *Sol. Energy Mater. Sol. Cells*, 2017, **1**, 370–376.

74 F. M. T. Enam, K. S. Rahman, M. I. Kamaruzzaman, K. Sobayel, P. Chelvanathan, B. Bais, M. Akhtaruzzaman, A. R. M. Alamoud and N. Amin, *Opt. - Int. J. Light Electron Opt.*, 2017, **139**, 397–406.
75 S. Das, C. Frye, P. G. Muzykov and K. C. Mandal, *ECS Trans.*, 2012, **45**, 153–161.
76 G. Chen, J. Li, S. Chen, Z. Huang, M. Wu, J. Zhao, W. Wang, H. Lin and C. Zhu, *Mater. Chem. Phys.*, 2017, **188**, 95–99.
77 J. R. Vegelius, K. O. Kvashnina, H. Hollmark, M. Klintenberg, Y. O. Kvashnin, I. L. Soroka, L. Werme and S. M. Butorin, *J. Phys. Chem. C*, 2012, **116**, 22293–22300.
78 G. Chen, W. Wang, J. Zhao, W. Yang, S. Chen, Z. Huang, R. Jian and H. Ruan, *J. Alloys Compd.*, 2016, **679**, 218–224.
79 J. van Embden, K. Latham, N. W. Duffy and Y. Tachibana, *J. Am. Chem. Soc.*, 2013, **135**, 11562–11571.
80 C. D. Wagner, *Handbook of X-ray Photoelectron Spectroscopy*, Perkin-Elmer Corporation, Physical Electromics Division, Eden Prairie, 1979.
81 M. Kundu, T. Hasegawa, K. Terabe, K. Yamamoto and M. Aono, *Sci. Technol. Adv. Mater.*, 2008, **9**, 035011.
82 K. H. Park, J. Choi, J. Chun, H. J. Kim and S. U. Son, *Chem. Commun.*, 2008, **14**, 1659–1668.
83 H. Yang, M. Li, L. Fu, A. Tang and S. Mann, *Sci. Rep.*, 2013, **3**, 1336.
84 R. Delobel, H. Baussart, J.-M. Leroy, J. Grimblot and L. Gengembre, *J. Chem. Soc. Faraday Trans. 1 Phys. Chem. Condens. Phases*, 1983, **79**, 879–891.
85 W. E. Morgan, W. J. Stec and J. R. Van Wazer, *Inorg. Chem.*, 1973, **12**, 953–955.
86 R. Reiche, D. Dobler, J. . Holgado, A. Barranco, A. . Martín-Concepción, F. Yubero, J. . Espinós and A. . González-Elipe, *Surf. Sci.*, 2003, **537**, 228–240.
87 Q. Ni, D. W. Kirk and S. J. Thorpe, *ECS Trans.*, 2013, **50**, 87–94.
88 B.-Y. Su, S.-Y. Chu, Y.-D. Juang and H.-C. Chen, *Appl. Phys. Lett.*, 2013, **102**, 192101.
89 W. Jaegermann, A. Klein and T. Mayer, *Adv. Mater.*, 2009, **21**, 4196–4206.
90 Z. C. Feng, H. C. Chou, A. Rohatgi, G. K. Lim, A. T. S. Wee and K. L. Tan, *J. Appl. Phys.*, 1996, **79**, 2151–2153.
91 J. Fritsche, A. Klein and W. Jaegermann, *Adv. Eng. Mater.*, 2005, **7**, 914–920.
92 I. Repins, M. A. Contreras, B. Egaas, C. DeHart, J. Scharf, C. L. Perkins, B. To and R. Noufi, *Prog. Photovolt. Res. Appl.*, 2008, **16**, 235–239.
93 D. Schmid, M. Ruckh, F. Grunwald and H. W. Schock, *J. Appl. Phys.*, 1993, **73**, 2902–2909.